

Solar Active Region Coronal Jets II: Triggering and Evolution of Violent Jets

Alphonse C. Sterling¹, Ronald L. Moore^{1,2}, David A. Falconer^{1,2}, Navdeep K. Panesar¹,
and Francisco Martinez³

ABSTRACT

We study a series of X-ray-bright, rapidly-evolving active-region coronal jets outside the leading sunspot of AR 12259, using *Hinode*/XRT, *SDO*/AIA and HMI, and *IRIS* data. The detailed evolution of such rapidly evolving “violent” jets remained a mystery after our previous investigation of active region jets (Sterling et al. 2016, Paper 1). The jets we investigate here erupt from three localized subregions, each containing a rapidly evolving (positive) minority-polarity magnetic-flux patch bathed in a (majority) negative-polarity magnetic-flux background. At least several of the jets begin with eruptions of what appear to be thin (thickness $\lesssim 2''$) miniature-filament (minifilament) “strands” from a magnetic neutral line where magnetic flux cancelation is ongoing, consistent with the magnetic configuration presented for coronal-hole jets in Sterling et al. (2015). Some jets strands are difficult/impossible to detect, perhaps due to, e.g. their thinness, obscuration by surrounding bright or dark features, or the absence of erupting cool-material minifilaments in those jets. Tracing in detail the flux evolution in one of the subregions, we find bursts of strong jetting occurring only during times of strong flux cancelation. Averaged over seven jetting episodes, the cancelation rate was $\sim 1.5 \times 10^{19}$ Mx hr⁻¹. An average flux of $\sim 5 \times 10^{18}$ Mx canceled prior to each episode, arguably building up $\sim 10^{28}$ – 10^{29} ergs of free magnetic energy per jet. From these and previous observations, we infer that flux cancelation is the fundamental process responsible for the pre-eruption buildup and triggering of at least many jets in active regions, quiet regions, and coronal holes.

¹NASA Marshall Space Flight Center, Huntsville, AL 35812, USA,
alphonse.sterling@nasa.gov, ron.moore@nasa.gov

²Center for Space Plasma and Aeronomic Research, University of Alabama in Huntsville, AL 35899, USA

³Georgia State University, Atlanta, GA, USA

Subject headings: Sun: activity — Sun: filaments — Sun: flares — Sun: magnetic fields — Sun: UV radiation

1. Introduction

Solar coronal jets are dynamic features that grow to long lengths compared to their widths. They occur in all solar environments: quiet Sun, coronal holes, and the edges of active regions (Raouafi et al. 2016). *Yohkoh*'s soft X-ray telescope (SXT) primarily saw them in active regions (e.g. Shibata et al. 1992; Shimojo et al. 1996), while *Hinode*'s X-ray telescope (XRT) found them to be plentiful in polar coronal holes also (Cirtain et al. 2007). In polar coronal holes they typically reach heights of $\sim 50,000$ km and widths of ~ 8000 km, occurring at a rate of ~ 60 /day in the two polar holes, and having lifetimes of ~ 10 min (Savcheva et al. 2007). Pucci et al. (2013) found such jets to have energies $\sim 10^{26}$ – 10^{27} erg for the hotter component of the jet, and they point out that the chromospheric/cool-coronal jet that sometimes accompanies the hot component (Moore et al. 2010, 2013) could increase this by about an order of magnitude. In a study weighted toward active region jets (where 68% of 100 jets occurred in active regions, and the others in either coronal holes or quiet Sun), Shimojo et al. (1996) report: a large range of lengths, averaging 1.5×10^5 km; a large range of lifetimes, going from ~ 100 s to ~ 4 hrs; and outward velocities ranging over 100–400 km s $^{-1}$, with an average of 200 km s $^{-1}$. For a sample of jets, Shimojo & Shibata (2000) found energies of $\sim 10^{27}$ – $\sim 10^{29}$ erg. Independent of where they occur on the Sun, essentially all coronal jets observed in X-rays appear as a bright spire with a base brightening, often with the brightest part of the base sitting on one side of the base; we call this a jet-base bright point (JBP). (In EUV images the JBP is also usually apparent as a sharp brightening, although at times it does not stand out as distinctly as it does in X-rays, due to factors such as the details of the EUV passbands and the possible presence of obscuring cooler-temperature material.)

Explaining the JBP in addition to the spire has been a key aspect of proposed physical mechanisms for what produces the jets. An early suggestion was that newly emerging magnetic flux elements reconnecting with ambient coronal fields produces the jets (e.g., Shibata et al. 1992; Yokoyama & Shibata 1995). This emerging-flux model for coronal jets was put forth when the best data available in which to see jets were X-ray images, and the cadence and regularity of magnetic data was limited. More recent data sources, such as the multiple-EUV-wavelength images from the Atmospheric Imaging Assembly (AIA) and the regular and high-cadence magnetograms from the Helioseismic and Magnetic Imager (HMI), both on the Solar Dynamics Observatory (*SDO*) satellite, have made it possible to examine

the origins of coronal jets in greater detail. Images from AIA show that, at least in many cases, the jets originate from the eruption of a small-scale filament (e.g. Shen et al. 2012; Liu et al. 2014; Adams et al. 2014; Sterling et al. 2015); following earlier works, we will call these small-scale filaments “minifilaments.” Figure 1 shows a schematic of the minifilament-eruption jet-production process as proposed by Sterling et al. (2015).

This minifilament-eruption picture however was originally developed from observations of polar coronal hole jets (Sterling et al. 2015). We have recently found the picture also to hold for quiet Sun coronal jets (Panesar et al. 2016a). Sterling et al. (2016) (Paper 1 hereafter) investigated whether *active region jets* also typically follow the Figure 1 scenario, and the findings were mixed. They observed several jets, and found that at least three of them showed characteristics of the minifilament-eruption scenario. These three jets were studied in detail in Paper 1; they showed relatively slow development, with a cool-material minifilament well-resolved by AIA in time and space as it moved toward eruption and jet formation. Two of these events made a surge and a spray, but showed either a relatively weak signature or no obvious signature in available X-ray images (obtained from the Soft X-ray Imager, SXI; *Hinode* XRT data not being available). The third slowly evolving jet did produce a stronger X-ray signature, although still modest compared to other jets. All three of those three jets could be understood with the minifilament-eruption interpretation of Figure 1. In addition however, there were several jets that made strong SXI X-ray jets (originating from region “C” of Fig. 3(a) in Paper 1). Paper 1 did not determine the origin of those jets because they were fast-developing and/or because their early-development stages were obscured by surrounding material. In this paper we refer to such fast-developing jets as “violent” active region jets, to distinguish them from the easier-to-decipher more-gradually-developing jets that clearly resulted from erupting minifilaments. Paper 1 was however able to conclude that those violent jets did occur at a neutral line that showed unambiguous flux cancelation.

Thus, from the Paper 1 study, the question of whether those comparatively violent jets follow the minifilament-eruption scheme was unresolved. Here we revisit this question by studying similarly violent jets from a different active region. We use a broader range of data than in the previous study, including images from the *Hinode* X-ray telescope (XRT) and from the Interface Region Imaging Spectrograph (*IRIS*) instrument, as well as *SDO/AIA* and HMI, to assist with trying to unravel the nature of these violent active region coronal jets.

2. Instrumentation and Data

For our investigations we use *SDO/AIA* (Lemen et al. 2012) images in seven EUV wavelength bands: 304 Å, 171 Å, 193 Å, 211 Å, 131 Å, 94 Å, 335 Å, and in one UV band: 1600 Å. Each of these channels tends to detect plasma emissions within a limited temperature range determined by characteristic emission lines around these wavelengths, although in some cases there can be two or more such characteristic temperatures; see Lemen et al. (2012) for details. *AIA* observes the full Sun, has detectors with $0''.6$ pixels, and nominally operates with a cadence of 12 s in the EUV channels and 24 s in the UV channels. *Hinode/XRT* (Golub et al. 2007) has a broadband response in the X-ray range to emissions from plasma hotter than about 1.0×10^6 K. It has $1''.02$ pixels, and normally observes the Sun with a limited field of view (FOV) and with varying cadences. *IRIS* (De Pontieu et al. 2014) does high resolution ($0''.17$ pixels) imaging in the UV range with its slit-jaw camera, with four different filters: 1330 Å (C II, 30,000 K) and 1400 Å (Si IV, 65,000 K) with a 40 Å bandpass each, and 2796 Å (Mg II k, 15,000 K) and 2831 Å (Mg II h/k wing, 6,000 K) with a 4 Å bandpass each. For the time period we investigate in Section 4 below, slit-jaw images are available in all but the 2831 Å line.

3. Data Set: Violent Jets in X-rays and in EUV

Our data selection is based on XRT observations from the second-half of the disk passage of NOAA AR 12259, from 2015 January 13 12:34 UT to January 20 06:30 UT. This is during a period of “focused mode” observations by *Hinode*, when relatively-long-term observations on selected targets are carried out. Although the XRT observations were not completely continuous over this period, there were long stretches of uninterrupted observations, typically at a cadence of ~ 5 min, although with some periods of higher cadence (30 s). Figure 2 shows the region in white light, along with a magnetogram. Over this period there were numerous X-ray jets occurring at the periphery of the region, with the jets tending to cluster in different locations of the region for extended periods of time. In this paper, we will focus on one such cluster of jets, occurring in the boxed region of Figure 2(a) over 2015 January 13-14.

Figure 3 shows sample XRT images of the region, and the accompanying animation shows the region over the full period of our observations. XRT had a gap in observations during the period, with the first set of observations running between 13 January 14:34 UT and 17:44 UT, and the second running nearly uninterrupted between 14 January 06:16 UT and 16 January 09:43 UT. For our investigations, we cut off this second block at 14 January 22:34 UT, because the jetting in the Figure 3 FOV largely ends around that time. From the animation accompanying Figure 3, one can see that the jets happened in the three subregions,

R1, R2, and R3 of Figure 3.

For the study of this paper, we examined jets occurring in the FOV of Figure 3 over the time period from 2016 January 13 14:30 UT to January 14 23:35 UT. We discuss in most detail (see Sect. 4 onward) jets of the R2 region for a more restricted period, on 2016 January 14 from 12:35 UT to 22:35 UT, when that region was particularly jet productive.

Figure 4 shows the three jetting regions in AIA EUV 193 Å and AIA 94 Å images, with and without overlaid HMI magnetograms. We also include accompanying two-minute-cadence movies that, different from the XRT movies of Figure 3, are uninterrupted over the entire time period of our observations. From these movies we can see that jets occur nearly continuously throughout the period, although there still is a quieter period on Jan 14 between about 16:00 UT and 17:20 UT, as is also apparent in the XRT movie.

Figure 5 shows an intensity lightcurve from the AIA 94 Å channel over the observation period, where we have integrated the intensity at each timestep over the FOV of the Figure 3 and Figure 4 images; thus this lightcurve shows the intensity variations over R1, R2, and R3 regions of Figure 3. If XRT had the cadence of AIA, some of the jets seen by AIA would undoubtedly have been detected by XRT in-between the times of some of those visible in the XRT animation accompanying Figure 3.

Unlike the active region jets of Paper 1, most jets of this study were not clearly identifiable in the *GOES* soft X-ray flux plots. This is largely due to a somewhat higher *GOES* background for these events; for the times of our events here the background is very near the C1 level, while for the events of Paper 1 the average background was at the high-B level. Additionally, at least one other region, AR 12257 at the west limb, was very active during this period, which might contaminate *GOES* emissions near the time of our identified jets. Two events identified by NOAA as flares that are likely in the base of our jets are a C1.6 and a C1.9 event at 01:54 UT and 10:38 UT, respectively, on 2015 January 14.

It is apparent from the 193 Å animation accompanying Figure 4(a) that fan loops that emanate from the sunspot on the south edge of the figure obscure much of the jet activity, making it difficult to see the locations of origin of many of the jets. Also, absorbing material, frequently retracting jet material, sometimes obscures observations of the jets; Paper 1 also identified this as a difficulty with trying to observe the origin of some of their jets.

Overlaying HMI magnetograms onto the images (Figs. 4(c) and 4(d)) shows that there is a mixture of polarities in the region. Overall, the dominant polarity is negative, but there are three islands of positive polarity, the minority polarity of the region. These three mixed-polarity regions coincide with the three X-ray-bright areas of Figure 3: R1, R2, and R3, and are the source of the bulk of the jets of the region over the time period covered by the movies

accompanying Figures 3 and 4. In the following we will first consider a set of jets occurring in region R2, and then we will consider examples of jets from the other locations.

4. Homologous Violent Jets from Subregion R2

Subregion R2 of Figure 3 shows particularly substantial jetting activity on January 14, with many of the jets apparently homologous. We first examine in detail a jet episode of January 14 that begins in XRT images near 14:40 UT. We select this particular event because we had excellent coverage of it; in addition to AIA and HMI data, we also have available *IRIS* slit-jaw images and high-cadence (~ 30 s) XRT images.

Figure 6 shows the jet region. Over the period of the high-cadence AIA movies accompanying Figure 6(a), there is actually a sequence of several repeated jets around the time of the strong one near 14:40 UT. From the animation accompanying Figure 6(a), each jet begins at an isolated location that becomes the eastern edge of the jet, near $(x,y)=(85,-150)$. A very weak jet starts at 13:50 UT and continues for about 7 min. Another starts from the same location at $\sim 14:07:11$ UT, with the emission from that developing jet remaining confined to a location with narrow extent in the east-west direction. It then however spreads toward the west with time, first gradually and then relatively explosively from 14:17 UT, and reaches a maximum extent of $\sim 15''$ at about 14:30 UT. As this jet episode is fading, the above-mentioned jet that starts at 14:40 UT in X-rays begins; in the AIA videos, its initial brightening starts at about 14:32 UT at the eastern location. It starts to broaden markedly from about 14:41 UT, reaches a maximum extent near 14:48 UT, and then fades. A new feature then brightens from 14:52 UT, but it is from a different origin site, and so is not homologous with the three events just described. But a new event, homologous with those three earlier events, does start at about 15:02 UT, although it is heavily obscured by foreground opaque material; it has a more complicated development that is still continuing as the Figure 6(a) high-cadence movie ends at 15:40 UT.

Figure 6(b) shows the magnetogram of the region, and Figure 6(c) shows an *IRIS* 1400 Å image of part of the FOV of the images in the earlier two panels. Figures 6(d)—6(f) show the *IRIS* image at three different times with the magnetogram contours overlaid. This sequence begins in Figure 6(d) with the above-mentioned event that started in AIA at 14:32 UT. It is clear that the eastern edge of the event is lodged into the neutral line between polarities B3 and B4 in Figure 6(d), with negative/positive polarities on the east/west side of the originating jet. On its southern edge the jet may again be bounded by a less-well-defined neutral line that includes the positive flux clump labeled B6 in Figure 6(d). Figure 6(f) shows the jet at near its maximum extent; at this time its western edge is lodged in a region

of negative polarity.

We can make a direct comparison between the *IRIS*-observed jet and magnetograms in Figures 6(d)—6(f), and the jet schematic of Figure 1. In both the schematic and in the observations, the dominant polarity is negative and the minority polarity is positive. In the schematic, the jet starts between the respective negative and positive polarities “A” and “B” of Figure 1(c), and then in time the jet spreads horizontally out to polarity “C.” Similarly, in the observations, the jets starts between B3 and B4 (Fig. 6(d)), and spreads out to the location of B5 (Fig. 6(f)). Therefore, the observations of this active region jet are broadly consistent with the schematic of Figure 1, which was drawn based on observations of coronal hole jets. We also inspected other available *IRIS* slit-jaw wavelengths for this event, and they are consistent with what we find from the 1400 Å images.

One question about this comparison between these violent active region jet observations and the Figure 1 schematic however is whether there is a minifilament that erupts from the Figure 6(d) B3—B4 neutral line to form the jet, as presented in the Figure 1 schematic. In AIA EUV images, for the jet episode beginning at about 14:07 UT, we can identify strands of absorbing material erupting from the B3—B4 neutral line. One such strand is touched by the tip of the black arrow in the 171 Å image in Figure 6(a); it has width $\lesssim 2''$. A similar such strand is discernible in a subsequent jetting episode in the video accompanying Figure 6(a) at times around 14:41:23 UT. When viewed against the disk however, filament material is apparently difficult to see in *IRIS* slit-jaw images, reportedly being semi-transparent and optically thin in 1330 Å and 1400 Å images (Li & Zhang 2016). Consistent with this, we see no absorbing filament material at those slit-jaw wavelengths, nor do we see any such material in the 2796 Å slit-jaw images. Nonetheless, the AIA 171 Å (and also 193 Å) observations are suggestive of ejections of cool minifilament material in narrow, long strands. While these features are only marginally apparent here, we will show cases below (Section 5) where thin filament-like strands appear more clearly than here.

Also to be consistent with the Figure 1 schematic, a JBP should occur along the B3—B4 neutral line. We identify candidate brightenings in AIA 94 Å images (video accompanying Fig. 4(b)), e.g. at 14:16:01 UT and again at about 14:40:01 UT and about 15:16:01 UT in the video accompanying Figures 4(b) and 4(d). This brightening is also apparent in X-rays, e.g. on Jan 14 at 14:20:52 UT, 14:44:32 UT, and at 15:19 UT in the video accompanying Figure 3; the location of this brightening matches that of the JBP in the Figure 1(b)—1(c) schematic. Our observed candidate brightenings however are soon superseded in brightness by neighboring loops rooted in stronger magnetic fields.

Similarly, we expect new bright loops connecting the minifilament-eruption location, i.e. the minority-polarity flux near the B3—B4 neutral line, with the majority-polarity roots of

the neighboring larger loop in the Figure 1 schematic, at the times of Figures 1(c) and 1(d). Such connections are repeatedly identifiable in the AIA 94 Å video accompanying Figures 4(b) and 4(d) at, e.g., on Jan 14 around 14:26:01 UT, 14:46:01 UT, and at 15:26:01 UT, respectively with the brightenings listed in the previous paragraph. These connections also are apparent in the *IRIS* image in Figure 6(f), where the jet intensity brightenings clearly extend from the positive-polarity side of the B3—B4 neutral line to the B5 negative-polarity region. In each of these cases, the lateral extent of bright emitting jet material expands to cover the approximate extent of the base region, consistent with the shadings in Figure 1(c) and 1(d).

This spire expansion with time is also apparent in the XRT X-ray video accompanying Figure 3, especially for the higher-cadence observations of the jet over 14:41 UT—14:51 UT, and thus conforms to the definition of blowout jets presented in Moore et al. (2010, 2013). Moreover, a prediction of the minifilament-eruption scenario is that the jet spire should move away from the JBP location with time (Sterling et al. 2015); this direction of movement is clearly visible in the XRT movie (and other movies) for this jet.

We conclude that for the time interval of the *IRIS* movie of Figure 6 (approximately 14:48 UT—15:25 UT on Jan 14), in most respects the jets originating at the B3—B4 neutral line (labeled in Fig. 6(d)) follow the schematic of Figure 1. Possible differences however are that the emission at the expected JBP is soon dominated in brightness by emissions from neighboring stronger-field loops. Also, we are not able to determine unambiguously whether there is a cool-material minifilament ejected at the start of the eruption. We do observe narrow strand-like absorbing features near the AIA spatial-resolution limit, that are embedded/entrained in bright jetting material, and could be an erupting minifilament. We next consider other jets in the same active region where such strands unambiguously participate in the jet development in the manner depicted in Figure 1.

5. Violent Jet Eruptions Displaying Obvious Erupting Minifilaments

In Section 4 we focused on events for which we had the best mutual coverage among XRT and *IRIS*, in addition to AIA and HMI. Those jets however did not show clearly an accompanying minifilament eruption. Many other jets however occur among the three bright areas of this active region depicted in Figure 3. From the low-cadence AIA 193 Å video accompanying Figure 4(a), we can identify several cases where we can discern minifilaments erupting in step with the jet more clearly than in the examples of Section 4.

Figure 7 shows two such jets; although XRT and *IRIS* data are not available at these

times, we present AIA 193 Å images in Figure 7 and 12 s-cadence images in the accompanying animations. There are two successive jet eruptions, respectively starting at $\sim 01:34$ UT and at $\sim 01:50$ UT. In this case the jets originate from subregion R1, and specifically from the B1—B2 neutral line and spread out to the B3 polarity (Fig. 7(d); see Fig. 6(d) for labels). This is in contrast to the situation in Figure 6, where the jets originated in subregion R2, and specifically from the B3—B4 neutral line, and spread out to the B5 polarity. That is, for the events of both Figures 6 and 7, the jets form with a positive-flux minority-polarity setup. In the Figure 6 case that positive polarity is B4, and in the Figure 7 case that positive polarity is B2. Thus in Figure 7, in comparing with the labeling of the Figure 1(c) schematic, locations B1, B2, and B3 correspond to locations “A,” “B,” and “C” of the schematic, respectively.

Polarities of these subregions however are rapidly evolving. So at the time of Figure 7 the positive-polarity patch labeled B4 in Figure 6(d) has not yet formed, and by the time of Figure 6 the negative-polarity patch labeled B1 in Figure 7(d) is no longer present. We will discuss these rapid evolutionary magnetic changes in Section 6 below.

In contrast to the events of Section 4, here *we can discern clearly* an erupting minifilament in the magnetic eruption that drives each jet. From the Figure 7(a) video, this minifilament becomes discernible from the background dark material from about 01:29:06 UT. It then “crawls up” the neighboring mound-like bright region, corresponding to the time period between the schematics in Figures 1(a) and 1(b), until about 01:31:42 UT. It then starts moving (approximately) radially outward from the surface along what is to become the jet spire; this upturn in the minifilament’s trajectory occurs at a time corresponding to that between the schematics in Figures 1(c) and 1(d). In the animation accompanying Figure 7(a), dark material from the outward-moving minifilament quickly becomes engulfed in surrounding hotter jet material; this hotter material, represented by the shaded regions in Figures 1(c) and 1(d), is expected to form when field enveloping the field threading the cool minifilament material undergoes external reconnection with far-reaching field of the majority polarity, which is negative in both the observations and in the schematic. As with the jet of Figure 6, in this case the jet spire also starts out relatively narrow (e.g., at 01:35 UT), but then expands to span much of the mound-like bright region (e.g., at 01:37 UT), corresponding to the situation of the schematic in Figure 1(d). Again, in accordance with that schematic, the expansion is in a direction away from where the minifilament originally resides prior to its eruption.

For the second jet in the movie of Figure 7, the filament is even more obvious, first appearing at about 01:45:06 UT, and starting to erupt upward from about 01:50:18 UT.

These minifilaments appear to be strands of width $\lesssim 2''$. This is the same size range we inferred for jets of Figure 6 also, but they are much more obvious (darker) for these Figure 7

events. This could possibly be due to a better perspective in this case; here we are viewing region R1 instead of R2, allowing us to see more of the minifilaments as they crawl up the neighboring mound-like regions. Another factor could be that in the case of Figure 7 we can see the minifilaments before much of the external reconnection occurs between the field enveloping the minifilament and the surrounding coronal field; the hot emissions from that reconnection tend to create very bright jet-spire and large-lobe-loop material that blinds our view of the cooler material.

We have also inspected 12 s-cadence AIA 94 Å images of this same event in order to confirm the location of the JBP, but the findings regarding this are equally apparent in the 193 Å images of Figure 7 and its accompanying video, and thus we do not include the 94 Å images for this case. Based on the schematic of Figure 1, we expect the JBP to occur at the B1—B2 neutral line. For the first of the two jetting episodes, there is only very weak brightening in 193 Å at this location at about 01:20:54 UT. For the second jet episode, brightening at this neutral line (e.g., over approximately 01:48 UT—01:52 UT) is a little stronger than in the first episode.

In both episodes however, the strongest base brightening occurs $\sim 5''$ — $10''$ further to the west of the B1—B2 neutral line from which the minifilament strand originates. For the first jet episode this strongest brightening is at about 01:37:30 UT. For the second jet episode, at the time of the strongest brightenings the images are too saturated to make a reliable match to the magnetogram, but at, e.g., 02:18 UT, it is clear that the main base brightening is west of the B1—B2 neutral line. In both cases, these brightenings are strongest at about the time the minifilaments lift off radially away from the surface. For these jets, B2 is a strong positive polarity, and it is surrounded by other negative elements in addition to B1, including the negative-polarity patch B3, and negative patches north, south, and southeast of B3. These brightening locations are consistent with them being intense newly-formed loops from the external reconnection of the envelope of an erupting minifilament flux rope, corresponding to the red loop connecting polarities B and C in Figure 1(c); they are particularly bright because the flux elements in which those loops are rooted are particularly strong.

Another possibility is that the strong brightenings west of the B1—B2 neutral line is actually a secondary-jet-causing eruption, triggered by the filament eruption from the B1—B2 neutral line. In that case, that brightening would form the JBP for another jet, with the neutral line of that JBP being between the positive patch B2 in Figure 7(d) and negative polarity south of B2 (and thus these would correspond respectively to B and A in Fig. 1(c)), and the larger lobe field would be formed by B2 and the negative field north and east of B2 (these would correspond respectively to B and C in Fig. 1(c)).

Which, if either, of these explanation explains the strong intensity of the loops west

of the B1—B2 neutral line would require more investigation to determine with confidence; those investigations are beyond the scope of the present study.

We present one more example where we can identify an erupting minifilament, this time for an eruption occurring in region R3 of Figure 3. *IRIS* data are not available for this event. We do not present separate AIA high-cadence movies of this event, but from the video accompanying Figure 4(c), over January 14 10:22 UT—10:36 UT there is a minifilament (of width $\sim 5''$) moving in the southwest direction away from the neutral line north and east of positive magnetic clump labeled B7 in Figure 6(d). Subsequently this minifilament erupts outward, apparent in the video from 10:36 UT to 10:42 UT. From Figure 4(d), and its accompanying video at 10:38 UT, we see brightenings at the approximate location of the neutral line from where the minifilament erupted. Again the brightest location is shifted somewhat, in this case to the southern portion of the neutral line where the fields along that neutral line are strongest; but the brightening also extends further west of that neutral line, on top of the central portion of the B7 positive-polarity clump and negative field to its south. Similar brightenings are visible in X-rays in the XRT video accompanying Figure 3, over 10:36 UT—10:37 UT. Subsequently, the western brightening becomes extremely intense (apparent after saturation has subsided in the Fig. 3 XRT video at 10:53:46 UT). This again could be a very bright loop from the external reconnection, rooted in strong field.

6. Magnetic Field Evolution

From the above observations, apparently the factor responsible for the jetting occurring in the regions labeled R1, R2, and R3 in Figures 3(a) and 4(c) is the presence of the minority-polarity positive regions in the overall dominant-polarity negative field in the northwest portion of the active region. This is in accord with the general picture for jets presented in the schematic of Figure 1. Next we examine the evolution of the magnetic flux patches over a period of jetting in subregion R2.

From the video accompanying Figure 6(b), we see that rapid evolutionary changes, including flux emergence and flux cancelation, are occurring throughout the observation period. In order to make tractable investigation of the relationship between the magnetic changes and the jets, we limit our focus to the period when jetting is concentrated in region R2 of Figure 3; based on, e.g., the Figure 6 video, we see that the time window on 2015 January 14 over 12:35 UT—22:35 UT contains most of these R2 jets.

Figures 8(a) and 8(b) display the magnetic evolution over the time period, where the top two panels corresponding to the two parallel rectangular boxes in Figure 6(b), with

Figures 8(a) and 8(b) respectively corresponding to boxes (b1) and (b2) in Figure 6(b). Figures 8(a) and 8(b) show distance-time plots, where the vertical-axis distance runs along the x' axis in Figure 6(b), and the plotted quantity is the sum of the signed flux in the y' direction: $\int B dy'$. These Figure 6(b) boxes were selected and oriented so that we could follow the evolution at the source neutral line for the jets of region R2 of Figure 3, and also so that the x' direction would approximately be aligned with the drift direction of the positive-polarity clumps. We selected these two boxes rather than a single box covering the full area of b1+b2, because the positive flux of this R2 area approximately splits into two different clumps, each approximately contained in one of these two boxes, over the time period of Figure 8; one can see this from the animation accompanying Figure 6(b), which shows these two boxes overlaid over the time period of Figure 8. It is nonetheless hard to isolate the white flux completely over the full time range of Figure 8 and still show the features that we wish to highlight. Thus there is some drift of positive flux into box (b1) over 16:30 UT—18:30 UT; this increases the value of the positive flux contribution to the integral over dy' , and this accounts for a modest increase in the white intensity in the Figure 8(b) plot over this time.

Figure 8(c) shows the integrated intensity as a function of time of the blue box of Figure 6(b), and shows peaks at times of jet brightenings originating from region R2 of Figure 2. There is a cluster of jetting between about 13:45 UT and 15:45 UT, and a weaker cluster between about 20:00 UT and 22:30 UT, with the times indicated by the blue and magenta line pairs; these clusters of jets at the R2 location are apparent in the movies accompanying Figure 4. Both of these cluster times correspond to times of unmistakable flux cancelation at the main neutral line of region R2 in Figure 4(c), as can be seen by referencing the colored-line pairs in Figures 8(b).

A strong jet near 19:00 UT in Figure 8(c) corresponds to cancelation visible in Figure 8(a), highlighted by pairs of orange lines in both panels. This cancelation does not stand out as much as those in Figure 8(b); examining the movie accompanying Figure 6(b) shows that this is because, even though flux cancelation occurs at the neutral line, a strong positive flux element still remains immediately adjacent to the canceling neutral line. In summary, all of the main jets of this R2 subregion occur at the sites of flux cancelation.

Figure 9 shows the change with time of the total positive-polarity flux in each of the two boxes of Figure 6(b). Since some positive flux does enter into the box with time, we cannot trust in detail the flux changes over all times, due to the aforementioned positive-flux drifts into the boxes; but this effect seems to be small even over the time of the most obvious such drift into the box, 16:30 UT—18:30 UT. From the movie accompanying Figure 6(b), drifts of positive flux out of the boxes (b1) and (b2) appear to be even less extreme. Cancelation

in box (b1) corresponds to the times of enhanced jetting activity over approximately 14:00–16:00 UT (blue lines in Figs. 8 and 9) and over approximately 21:00–23:30 UT (magenta lines), and cancelation in box (b2) corresponds to the jet near 19:00 UT (orange lines). (Although prominent in AIA images, that 19:00 UT jet was not observed by XRT due to a gap in the observations.) Therefore these plots confirm our interpretation above that flux cancelation is taking place near the times of the jets.

We see in Figure 9(a) a rate of flux decrease of $\sim 0.5 \times 10^{19}$ Mx hr⁻¹ for about an hour around the time period where there is one outstanding jet in the AIA 94 Å intensity plot of Figure 8(c). For the period over 14:00–15:00 UT in Figure 9(b) the drop rate is $\sim 1.5 \times 10^{19}$ Mx hr⁻¹, and from Figure 8(c) we see that over that same time period (14:00–15:00 UT) there are about three main intensity peaks. (Especially for this 14:00–15:00 UT time window, we suspect that some cancelation is still occurring at the times when jets occur just before or after the times where the flux is dropping in Fig. 9(b), but that flux drop is not well-captured by the restricted box region of Fig. 6(b) we used to make that flux plot. This is why the blue lines in Figs. 8 and 9 cover a wider time window than just 14:00–15:00 UT for these jets.) From the videos accompanying Figures 4 and 6, the smaller peaks of Figure 8(c) over this time period are due to weaker jet events and/or secondary events. For the $\sim 21:00$ –22:30 UT period, there is a drop in flux with a rate of $\sim 1.8 \times 10^{19}$ Mx hr⁻¹, and over this time there are about three main jetting episodes identifiable in the Figure 8(c) light curve. Therefore we can say that the flux cancelation rates range over $(0.5\text{--}1.8) \times 10^{19}$ Mx hr⁻¹ for the active region jets that we observe over this R2 region over the period we examined. The average cancelation rate weighted by the number of jets at each of the above rates is $(1.5 \pm 0.5) \times 10^{19}$ Mx hr⁻¹, based on an average of about seven violent active region jets.

From this, we can estimate the amount of flux going into the buildup to each of these stronger jets (i.e., the jet activity corresponding to the three peaks in the Fig. 8(c) light curve). For the three such jets of the 14:00–15:00 UT 1-hr time window, this averages to $\sim 5 \times 10^{18}$ Mx. Similarly, for the three such jets the 21:00–22:30 UT 1.5-hr time period, the average is $\sim 4 \times 10^{18}$ Mx, and for the single jet of the ~ 1 -hr time period of the Figure 9(a) jet the average is also $\sim (4\text{--}5) \times 10^{18}$ Mx. So we can say that roughly $\sim 5 \times 10^{18}$ Mx of flux cancels prior to each of these stronger jet episodes. At least for subregion R2, upon which we performed the detailed analysis above, the jetting episodes continue until all of the clump of minority flux disappears.

7. Energetics

From the above-estimated amount of flux canceled prior to each of the jet episodes, we can make a rough estimate of the amount of energy in our active region violent jets, assuming that they are produced via erupting flux ropes as in the Figure 1 schematic.

We begin by estimating the size of the flux rope. We have already noted that the width of the erupting filament strands is $\lesssim 2''$; so let’s take a width $2r$ of $2''$. Figure 6(d) shows the length of the B3—B4 neutral line to be $\sim 10''$; we take this to be the length, l , of the flux rope, resulting in a ratio $l/r \sim 10$ for the flux rope. From this, we can derive a cross-sectional area, A , of the flux rope to be $\pi r^2 \sim 1.7 \times 10^{16} \text{ cm}^2$, and volume, V , to be $\pi r^2 l \sim 1.2 \times 10^{25} \text{ cm}^3$.

We estimate the magnetic field strength, B , of the flux rope by assuming that the total flux accumulated for each jet calculated above, $5 \times 10^{18} \text{ Mx}$, flows through the area of the flux rope, so that the total flux is BA . Taking that area to be the value A we estimated for the flux rope cross section, this yields $B \sim 300 \text{ G}$. This might be considered a rough estimate for B , considering that the flux rope would be expected to form nearer to the photosphere than at the time we observe erupting strands in the AIA images, and hence it would be more compact than what we calculated above, reducing A and increasing B somewhat; and on the other hand the true flux rope may have a cross-sectional area larger than that of the strand, for example if the strand has an enveloping cavity around it, reducing B somewhat. For an approximate upper limit for B , we use the value of the positive-polarity magnetic flux clumps that we measure from the magnetograms, such as B4 in Figure 6(d), where we find maximum values in the range 300 G—500 G. Thus we can consider a range for B of the flux rope to be approximately $\lesssim 300$ —500 G.

Using $B = 300 \text{ G}$ gives a magnetic energy in the flux rope $E_{fr} = V(B^2/8\pi) \approx 4.3 \times 10^{28} \text{ erg}$. Using our upper estimate for B would increase this by a factor of 3. Keeping in mind our caveats for our B values, we estimate the energy contained in the erupting-minifilament flux rope of the Figure 1 schematic to be $\sim 10^{28} \text{ erg} - 10^{29} \text{ erg}$ for the violent jets. Deductions from observations of jet energy values range over $10^{25} \text{ erg} - 10^{29} \text{ erg}$ (e.g. Shibata et al. 1992; Shimojo & Shibata 2000; Pucci et al. 2013; Raouafi et al. 2016), and so our derived estimate of flux rope energies is sufficient even for the greatest of these.

8. Summary and Discussion

We have examined a series of active region coronal jets, bright in X-rays and fast-evolving (“violent”), like the ones that were difficult to analyze in Paper 1. We find that the jets tend to occur in localized regions, which we initially identified in XRT soft X-ray images and

which we have labeled R1, R2, and R3 in Figure 3. Magnetograms show that each of these regions is broadly consistent with the schematic of Figure 1, where in each of R1, R2, and R3 there is a positive-polarity island butting up against a negative-polarity region, within a generally-negative-polarity larger region; that is, the positive and negative polarities are respectively the minority and majority polarities in the overall region. Figure 1 was initially drawn to describe jets in coronal-hole regions (Sterling et al. 2015), but recently we have found that it applies to jets in quiet Sun regions (Panesar et al. 2016a), and also to at least relatively-slowly-developing active-region coronal jets (Paper 1). Here we confirm that the same general picture also applies to at least many of the violent active region jets. We also found that cancelation occurs at the neutral line on which the jet activity commences, similar to what has been found in several other on-disk observations of coronal jets. In comparison with some other jets however, when detectable, minifilaments often appear as narrower ($\lesssim 2''$) and harder-to-see strands than our earlier-observed erupting minifilaments in jets in coronal holes and quiet regions.

We also found that loops neighboring the JBP can be more intense than the JBP. This phenomenon has however also been seen in some coronal hole jets (Moore et al. 2013), and therefore is not limited to the violent jets studied here. How this fits with the picture of the Figure 1 schematic (e.g. whether they form the JBP for a secondary jet) is a topic for later consideration.

In Figure 6 we examined in detail the set of jets occurring in the R2 region. High-cadence AIA EUV images and IRIS UV images overlaid with HMI magnetograms corroborate that the jets start with brightenings roughly along a strong-gradient neutral line between the minority and majority fluxes, that the minority-polarity region is linked by bright-loop extensions to farther-away majority-polarity regions, that the jet forms above this mixed-polarity setup, and that the jet spire drifts with time away from the location of the initial neutral-line brightenings; all of these properties are consistent with the minifilament-eruption schematic for jet production (Fig. 1).

For this same series of jets in region R2, we follow the magnetic evolution in Figures 8 and 9. We find that the jet occurrences cluster around times when the most-prominent flux cancelation is ongoing, and there are few strong jets (meaning those showing in the AIA 94 Å lightcurve of Fig. 8(c)) outside of those cancelation times. Thus, our results are consistent with the jets resulting from magnetic flux cancelation: when the strong cancelation episodes stop, the strong jetting stops. This is also consistent with recent findings for individual jets (e.g. Hong et al. 2011; Huang et al. 2012; Adams et al. 2014; Young & Muglach 2014a,b; Zhang & Ji 2014), and with recent findings examining multiple jets (e.g., Chen et al. 2015a,b; Panesar et al. 2016a). Other studies (e.g. Innes & Teriaca 2013) observe jet-like phenomena

originating from sites of network-field cancelation. Shelton et al. (2015) report jets resulting from flux emergence, although the flux changes provided in their figures also show flux decreases near the time of jet brightening, and so flux cancelation as the source of the jets in that case is not ruled out.

In some cases, jets do occur from locations of flux emergence. But for at least many of these cases, close examination shows that it is the cancelation of one pole of this emerging bipole with a nearby majority-polarity flux clump that results in the jet (e.g. Shen et al. 2012). Our active regions events here, and also those of Paper 1, also contain cases where flux emergence occurs, but as with Shen et al. (2012) the jets originate from the cancelation sites. In active regions especially, it is often difficult to separate emergence from cancelation, since both occur frequently during some times of the region’s life. In quiet Sun regions, cancelation consistently seems to be the source of the jets (Panesar et al. 2016a), even though in most cases the fluxes involved are long past their emergence phase. This leads us to suspect that, at least in many cases, *cancelation is the fundamental magnetoconvection process responsible for the pre-eruption buildup and triggering of jets*, even in active regions. It is conceivable that cancelations at much smaller rates at the edges of supergranular networks might produce even smaller scale jets, such as spicules (Sterling & Moore 2016).

As mentioned above, compared to many of the violent jets in active regions, minifilaments were easier to identify in the quiet Sun, coronal hole, and less-violent active-region-jet cases. For example, from the figures and animations of Panesar et al. (2016a), the quiet-Sun minifilament widths near their time of eruption onset are $\sim 2''\text{--}3''$, and from the figures and animations of Paper 1 the minifilaments leading to the weaker coronal jets (but producing surges/sprays) have widths of $\sim 3''\text{--}4''$. Here we have found harder-to-detect strands of what appears to be cool filament-like material of widths $\lesssim 2''$ in the eruption that drives the jet, akin to the minifilament eruptions in the less-violent jet eruptions. And in fact, with our new insights into observing these minifilament strands, we are also able to identify similar strands in the data for some of the violent jets of Paper 1.

Schmieder et al. (2013) also report observations of many threads along an active region jet, which may be the same features that we observe. They (Schmieder et al. 2013) suggest that the strands may not be a fully-erupting “flux rope.” Under this view, it may be that strands of a lower-laying minifilament structure “peel off” as strands, and erupt to form part of the jet. In our view this is plausible, whereby the peeling off would be triggered, somehow, by the flux cancelation that, from Figures 8 and 9, is clearly cotemporal with bursts of jet activity.

We found that observing these minifilaments/strands in active region jets is much more difficult than observing minifilaments in quiet Sun jets that we examined in Panesar et al.

(2016a). As suggested by Figure 7, even in relatively clear cases where we can see the erupting minifilament strands prior to jet-spire production, they can be hard to see without zooming in on the jet-base region and using high-cadence images.

Even in cases where we do not observe a minifilament or strand in the active region jets, we suspect that the same (Fig. 1) process occurs, but the absorbing material is not detected because of one or more of these reasons: (a) Its width is too small for us to resolve. (b) It is obscured by surrounding dark material. (c) It is surrounded by bright material resulting from internal reconnection of the legs of the field enveloping the erupting minifilament/strand, producing a bright “cocoon” (Sterling et al. 2011) wrapping around the erupting minifilament. Similarly, external reconnection between the minifilament/strand-enveloping field and the surrounding (relatively strong) ambient active region coronal field might produce a spire that is particularly bright (shaded regions of Figs. 1(c) and (d)), obscuring or partially obscuring the cool material. (d) The eruption may be occurring without cool material being ejected on the erupting field, just as some large-scale flux-rope eruptions occur without an obvious cool filament (and some of this bright material may result from brightening of the erupting (mini)filament material itself; see, e.g. Su et al. 2015). (e) A corollary to (d) is that, because the evolution of the magnetic fields is relatively fast in active regions compared to non-active regions, there may not be time for enough cool material to accumulate on a newly-formed flux rope for a substantial minifilament to develop. We do not know how quickly a (mini)filament can develop on a flux rope, but at least in the case of non-active-region filaments it can take a number of hours (e.g., Berger et al. 2012).

Regarding point (c), our observations do show that in the 304 Å images there is a mixture of brighter and darker strand-like features, and this is consistent with the minifilament material being partially obscured by brighter material during jet onset in some cases, and with that darker material enveloped by a brighter shell of material that has undergone reconnection and/or a bright spire.

Observations by Hong et al. (2016) using the New Vacuum Solar Telescope (NVST) show high-resolution $H\alpha$ images of an active region jet location reveal a very narrow (width $\sim 1''$) minifilament that erupts to form a jet similar to those observed here (cf. Panesar et al. 2016b), in agreement with the process described in Sterling et al. (2015) (Fig. 1). So erupting minifilaments of this size could be the erupting strands we observe. Also, observations by Li et al. (2015) of an active region jet show that it results when a filament, clearly visible in the NVST $H\alpha$ images, rises up and apparently reconnects with open field, with some of the filament material flowing out along the newly-open field lines. This process also could be responsible for the source of the erupting minifilament strands that we observe here. Sorting through these possibilities however is not possible for the cases we present here with the data sets we

use.

In conclusion: We observed X-ray coronal jets at the leading edge of an AR. The jets were in primarily three localized locations of the region. Those regions were where flux cancellation occurred, and the jets recurred at those respective locations until all of a clump of minority flux canceled and disappeared. The overall magnetic setup of all the observed jets agreed with that of the schematic presented by Sterling et al. (2015), which was originally drawn to describe coronal jets observed in polar coronal holes, where erupting minifilaments were found to be the source of the jets. There are however some differences from the situation with those coronal hole jets, as well as with coronal jets observed in quiet regions (which Panesar et al. 2016a, found to behave in a fashion similar to the coronal hole jets): In the case of AR jets (both here and in the previous study of AR jets in Sterling et al. 2016), clear minifilaments were frequently not apparent, and also the JBP’s intensity was frequently surpassed by brightenings from different enhanced-polarity locations of the jet’s base. We have put forth some ideas for why these differences exist. Our educated guess is that most AR jets work in the same manner as many non-AR jets, with apparent differences resulting from the environmental circumstances (such as stronger magnetic fields) or secondary eruptions/jets. Ultimately, further studies are needed to determine with certainty whether all coronal jets in all solar regions result from basically the same mechanism, or if instead there is a fundamental difference in the way jets of the different solar regions can be produced.

We thank K. Reeves for directing us to the data set we examined, and we thank J. Klimchuk and E. DeLuca for useful discussions. A.C.S., R.L.M., and D.A.F. were supported by funding from the Heliophysics Division of NASA’s Science Mission Directorate through the Heliophysics Guest Investigators (HGI) Program, and the *Hinode* project. N.K.P’s research was supported by an appointment to the NASA Postdoctoral Program at NASA MSFC, administered by Universities Space Research Association under contract with NASA. *Hinode* is a Japanese mission developed and launched by ISAS/JAXA, with NAOJ as domestic partner and NASA and STFC (UK) as international partners, and operated by these agencies in co-operation with ESA and NSC (Norway). FM was supported by NSF’s Research Experience for Undergraduates (REU) Program.

REFERENCES

- Adams, M., Sterling, A. C., Moore, R. L., & Gary, G. A. 2014, *ApJ*, 783, 11
- Berger, T. E., Liu, W., & Low, B. C. 2012, *ApJ*, 758, L37

- Chen, H., Zhang, J., Ma, S., et al. 2015, *ApJ*, 808, L24
- Chen, J., Su, J., Yin, Z., et al. 2015, *ApJ*, 815, 71
- Cirtain, J. W., Golub, L., Winebarger, A. R., et al. 2007, *Science*, 318, 1580
- Crooker, N. U., Gosling, J. T., & Kahler, S. W. 2002, *J. Geophys. Res.*, 107, 1028
- De Pontieu, B. et al. 2014, *Sol. Phys.*, 289, 2733
- Golub, L., Deluca, E., & Austin, G. et al. 2007, *Sol. Phys.*, 243, 63
- Hong, J., Jiang, Y., Zheng, R., Yang, J., Bi, Y., & Yang, B. 2011, *ApJ*, 738L, 20
- Hong, J., Jiang, Y., Yang, J., Yang, B., Xu, Z., & Xiang, Y. 2016, *ApJ*, 830, 60
- Huang, Z., Madjarska, M. S., Doyle, J. G., & Lamb, D. A. 2012, *A&A*, 548, A62
- Innes, D. E., & Teriaca, L. 2013, *Sol. Phys.*, 282, 453
- Lemen, J. R., Title, A. M., & Akin, D. J. et al. 2012, *Sol. Phys.*, 275, 17
- Li, T., & Zhang, J. 2016, *A&A*, 589, A114
- Li, X., Yang, S., Chen, H., & Zhang, J. 2015, *ApJ*, 814, 13L
- Liu, J., Wang, Y., Liu, R., Zhang, Q., Liu, K., Shen, C., & Wang, S. 2014, *ApJ*, 782, 94L
- Moore, R. L., Cirtain, J. W., Sterling, A. C., & Falconer, D. A. 2010 *ApJ*, 720, 757
- Moore R. L., Sterling A. C., Falconer D. A. & Robe D. 2013 *ApJ*, 769 134
- Panesar, N. K., Sterling, A. C., Moore, R. L., & Chakrapani, P. 2016a, *ApJ*, 832, L7
- Panesar, N. K., Sterling, A. C., & Moore, R. L. 2016b, *ApJ*, 822, 23L
- Pucci, S., Poletto, G., Sterling, A. C., & Romoli, M. 2013, *ApJ*, 776, 16
- Raouafi, N. E., Patsourakos, S., Pariat, E., et al. 2016, *SSRv*, 201, 1
- Savcheva, A., Cirtain, J. W., DeLuca, E. E., et al. 2007, *PASJ*, 59S, 771S
- Shelton, D., Harra, L., & Green, L. 2015, *Sol. Phys.*, 290, 753
- Schmieder B., Guo Y., Moreno-Insertis F. et al. 2013, *A&A*, 559, A1
- Shen, Y., Liu, Y. E., Su, J., & Deng, Y. 2012, *ApJ*, 745, 164

- Shibata, K., Ishido, Y., Acton, L. W., et al. 1992, PASJ, 44L, 173
- Shibata, K., Nitta, N., Strong, K. T., et al. 1994, ApJ, 431, L51
- Shimojo, M., Hashimoto, S., Shibata, K., Hirayama, T., Hudson, H. S., & Acton, L. W. 1996, PASJ, 48, 123
- Shimojo, M., & Shibata, K. 2000, ApJ, 542, 1100
- Sterling, A. C., Moore, R. L., & Freeland, S. E. 2011, ApJ, 731, L3
- Sterling, A. C., Moore, R. L., Falconer, D. A., & Adams, M. 2015, Nature, 523, 437
- Sterling, A. C., Moore, R. L., Falconer, D. A., et al. 2016, ApJ, 821, 100 (Paper 1.)
- Sterling, A. C., & Moore, R. L. 2016, ApJ, 828, 9
- Su, Y., van Ballegooijen, A., McCauley, P., Ji, H., Reeves, K. R., & DeLuca, E. E. 2015, ApJ, 807, 144
- Yokoyama, T., & Shibata, K. 1995, Nature, 375, 42
- Young, P. R., & Muglach, K. 2014a, Sol. Phys., 289, 3313
- Young, P. R., & Muglach, K. 2014b, PASJ, 66, S12
- Zhang Q. M. and Ji H. S. 2014 A&A 561 A134

Fig. 1.— Schematic showing jet generation via minifilament eruption, as proposed in Sterling et al. (2015). This schematic is a modified version of that in Sterling et al. (2016) (Paper 1). (a) A minority-polarity (positive in this example) flux clump sits inside of a majority-polarity (negative) ambient background field. The positive polarity has connections to immediately-surrounding negative polarity field, naturally forming an anemone-shaped field pattern (Shibata et al. 1994) in 3D; these frames show a 2D cross section of the anemone. Here, the left side of the anemone contains a sheared, non-potential field; thus in 2D the structure consists of a small lobe adjacent to a larger lobe in this rendition (situations on the Sun might change the geometric ratios while maintaining the overall topology). In the picture, cool filament material (blue circle) gathers in the sheared field above and along this neutral line, analogous to filament formation on larger-scale sheared-field neutral lines; this is the minifilament. (b) Initiated by some (unspecified) trigger mechanism, the minifilament-carrying field (flux rope plus envelope) erupts outward, and travels between the larger lobe and the ambient field. This leads to magnetic reconnection (red X) interior to the erupting minifilament field (*internal* reconnection), making a flare loop (arcade in 3D) lower in the atmosphere (red semicircle); we identify this flare arcade with the observed JBP. (c) Upon reaching the field on the far side of the large lobe, the envelope of the erupting minifilament field reconnects with the ambient field (right-hand-side red X), making a new open field line (red open field line), and a new loop over the large lobe (large semicircular loop); the plasma on both of these newly-reconfigured field components is energized via heating and particle acceleration by the reconnection, and hence represented by the red color. (This is *external reconnection*, since it occurs external to the minifilament-flux-rope field that is driving the reconnection. This is also called interchange reconnection, e.g. Crooker et al. 2002.) Plasma pressure and magnetic force result in acceleration of hot plasma along the newly-opened field (orange shadings); we identify this heated plasma with the observed jet spire. In this frame, so far only the outer envelope of the erupting minifilament flux rope has undergone this reconnection, but the field threading the cool minifilament material has not, and so only a hot jet occurs so far. (d) As the minifilament eruption continues, the external reconnection can eat through the envelope field surrounding the cool minifilament material and the open field that threads that minifilament material. This cool material can then escape along that new open field, resulting in a cool (e.g., visible in AIA 304 Å images) jet, along side of or intertwined within the hot jet. Labels “A,” “B,” and “C” are referred to in the text to compare with magnetic polarities of observed jetting regions.

Fig. 2.— Overview of the jet-productive active region NOAA AR 12259, in *SDO*/HMI (a) white-light intensity, and (b) magnetogram images. In the magnetogram, black and white represent negative and positive polarities, respectively, with values greater (less) than 1000 G (-1000 G) saturated. The boxed region of (a) is a jet-prolific location over the period

of *Hinode*/XRT observations over 2016 January 13–14; jets of this study are concentrated in this region, and this boxed region is the field of view (FOV) of Fig. 4 below. For these, and for all other solar images in this paper, north is up and west is to the right, and the images have been differentially rotated to the common time of 2016 Jan 14 16:00 UT .

Fig. 3.— *Hinode*/XRT X-ray images of the boxed region of Fig. 2(a), with R1, R2, and R3 showing X-ray-bright subregions where multiple jets were concentrated over our observing period. Two different, but essentially homologous jets are occurring in subregion R2 in (a) and (b). Accompanying animations show that numerous jets occur over the XRT observing period. XRT was not observing this region over the time gap between 2016 Jan 13 17:44 and Jan 14 6:16 UT in the animation. (The abscissa in the animation prior to the time jump was artificially shifted to reflect the 2016 January 14 16:00 UT coordinate location; this was necessary because that location was outside of the XRT FOV at those observations times.)

Fig. 4.— AIA images of the jetting regions in (a) 193 Å and (b) 94 Å, and respectively the same in (c) and (d) but with HMI magnetogram contours overlaid (with overlay times given in parentheses in the title). Contour levels are at ± 30 , 50, 100, 750, and 1400 G, where red and green represent positive and negative polarities, respectively. Labels R1, R2, and R3 are above (north of) the neutral lines of the correspondingly-labeled regions in Fig. 3. Animations of these four panels are available.

Fig. 5.— Light curve of the AIA 94 Å intensity, integrated over the FOV of Figs. 3 and 4, at 2 min cadence. Peaks show incidences of flaring, often accompanied by jets, usually emanating from one or more of the subregions labeled R1, R2, and R3 in Fig. 3.

Fig. 6.— (a) AIA 171 Å image of a jet examined in §4, which was one of several homologous jets occurring in region R2 of Fig. 3. The tip of the black arrow points to a faintly visible erupting minifilament strand. (b) An HMI magnetogram of the region of (a), with values greater (less) than 300 G (-300 G) saturated. The dashed lines show the north and west edges of the FOV of the *IRIS* images in the subsequent panels. Boxes (b1) and (b2) inside of panel (b) show regions used to track magnetic development in Figs. 8 and 9, with the (x', y') coordinate system for those two boxes as indicated. The blue rectangle shows the region over which intensities in Fig. 8(c) are determined. (c) *IRIS* 1400 Å slit-jaw image of the jet of (a); the FOV is different from that of (a) and (b). (d–f) Same as (c), but with HMI magnetograms overlaid. The title of each of these three panels gives the time of the 1400 Å grayscale image, and in parentheses, the time of the magnetogram. Labels in (d) identify magnetic flux clumps, and are referred to in the text; a flux clump labeled B1 appears in Fig. 7, but that clump had disappeared by the time of this image. Animations of panels (a), (b), (c), and (d–f) are available. The animation corresponding to panel (b) runs twice, the

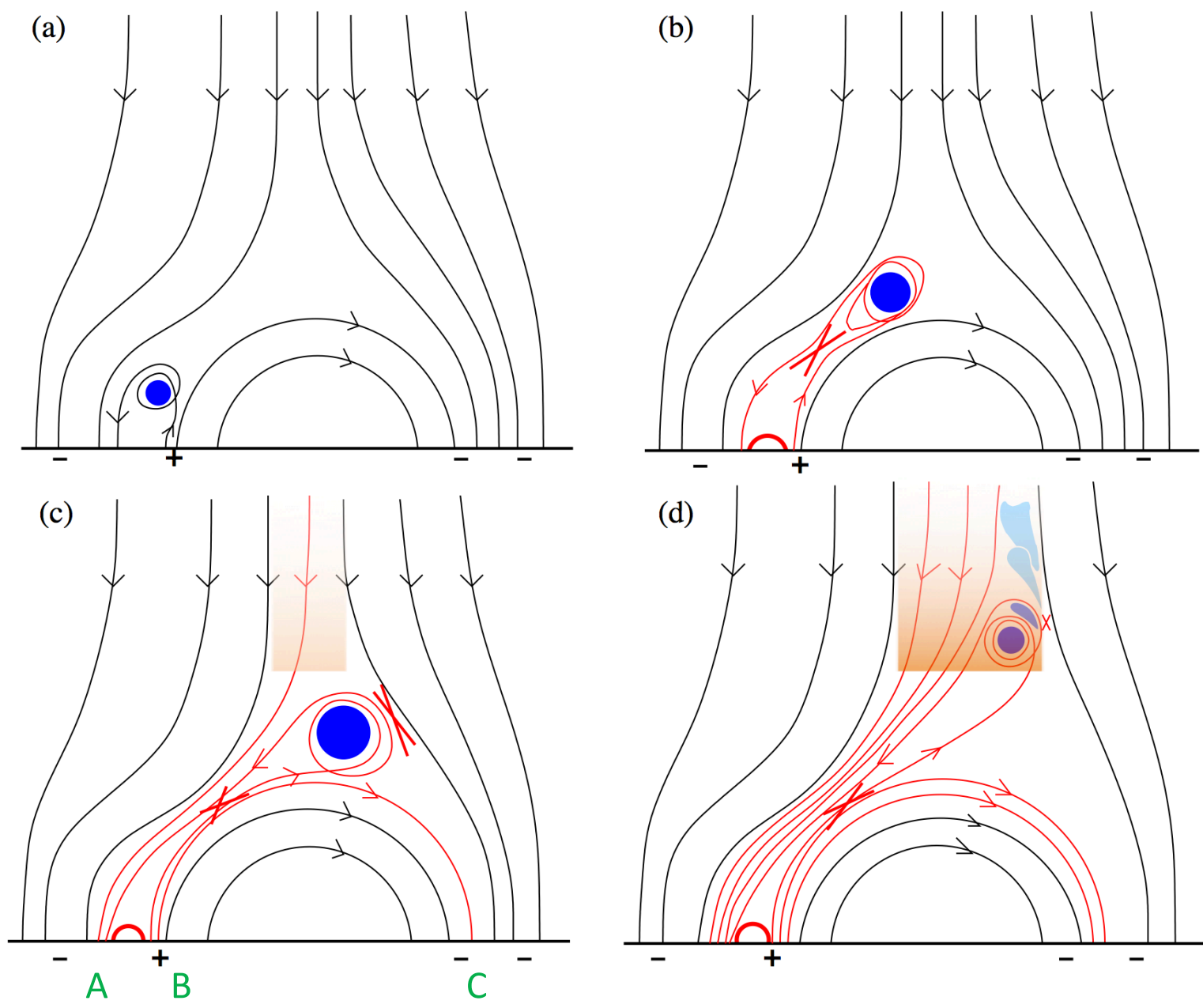
first time with only the magnetogram, and the second time with the boxes (b1) and (b2) overlaid for the time period corresponding to the plots in Fig. 9.

Fig. 7.— AIA 193 Å images showing minifilament “strands” at the start of a pair of jets from region R1 of Fig. 3, where (a) and (b) show the weaker of the two jets, and (c) and (d) show the stronger of the two jets. Arrows in (a) and (c) show the minifilament prior to eruption, at times when they are apparently “crawling up” a magnetic dome that has enhanced emission, corresponding to the large bipole in the Fig. 1 schematic. In (d), magnetogram contours, with properties of that in Fig. 4, are overlaid onto the region (with times given in parentheses in the title). Labels in (d) are as those in Fig. 4(c); region B1 appears here, but has disappeared by the time of Fig. 4. High cadence (12 s) animations of panels (a–c) and panel (d) are available.

Fig. 8.— Magnetic evolution over the times of the R2 region (labeled in Fig. 3) jetting. (a) Evolution in time of the magnetic elements in rectangular box labeled “(b2)” in Fig. 6(a), where the ordinate is distance along the x' axis of the rectangular box, and the abscissa is the net signed magnetic flux from integration along the y' direction of that rectangular box. (b) Same as (a), but for the rectangular box labeled “(b1)” in Fig. 6(b). (c) Light curve of the AIA 94 Å intensity, integrated over the blue box in Fig. 6(b), with 2 min cadence; peaks show the times of substantial jetting activity from region R2. Pairs of same-colored lines in (c) highlight times of two clusters of jets (blue and magenta), and of a strong single jet (orange). These correspond respectively to periods of flux cancelation in (b) and (a).

Fig. 9.— Magnetic flux changes with time, of the positive-flux clumps contained in the regions marked (a) box (b2), and (b) box (b1) in Fig. 6(b). Sharp drops in flux coincide with periods of increased jetting, as can be seen by comparing the identically-colored line pairs of Fig. 8(c) with the line pairs in this figure.

Figure 1



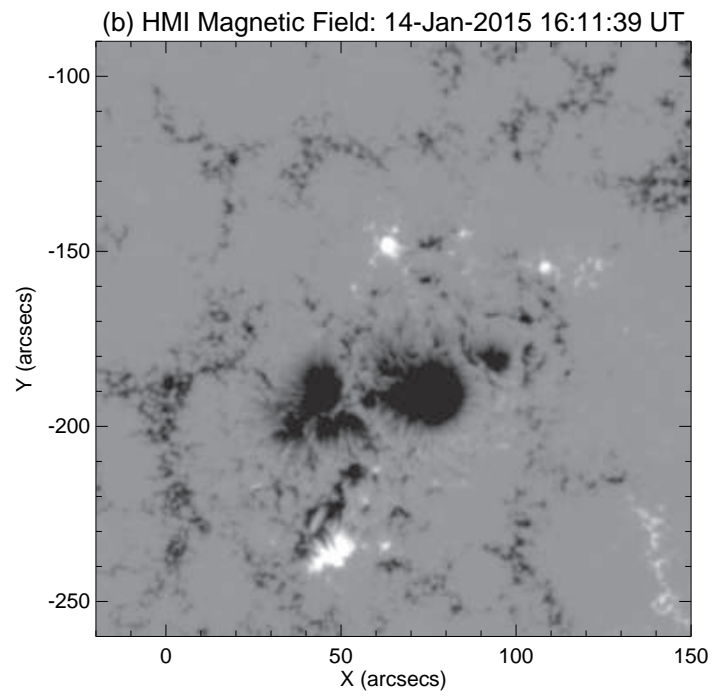
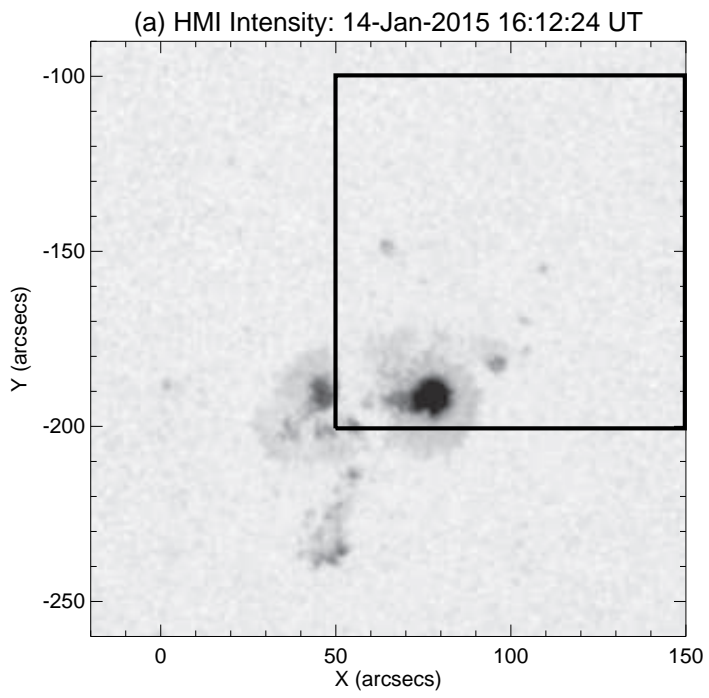


Figure 2

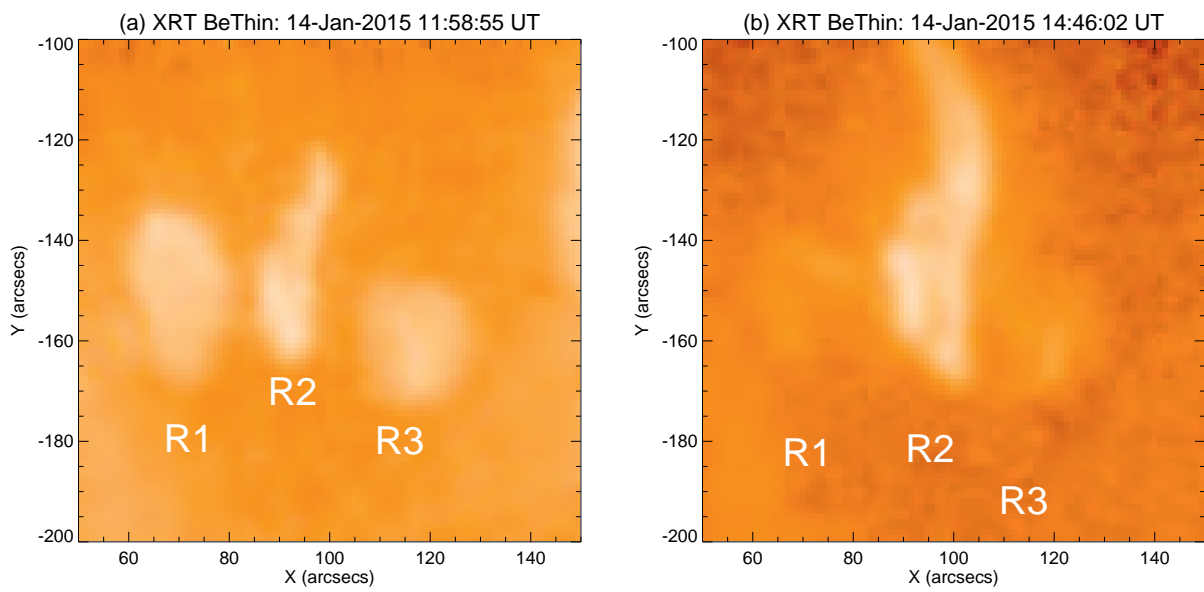


Figure 3

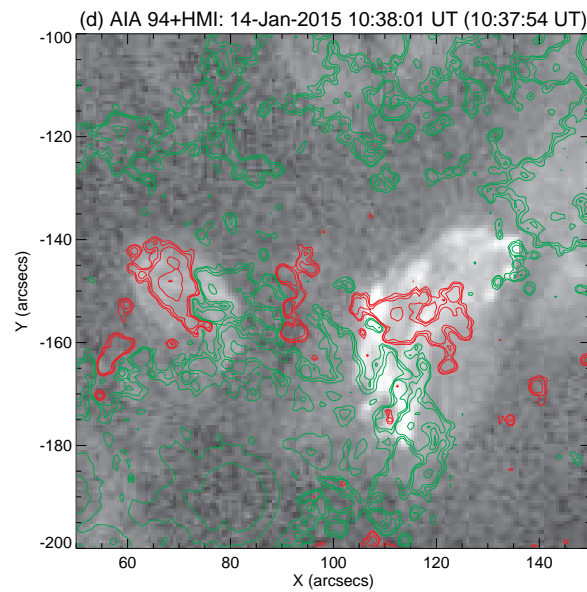
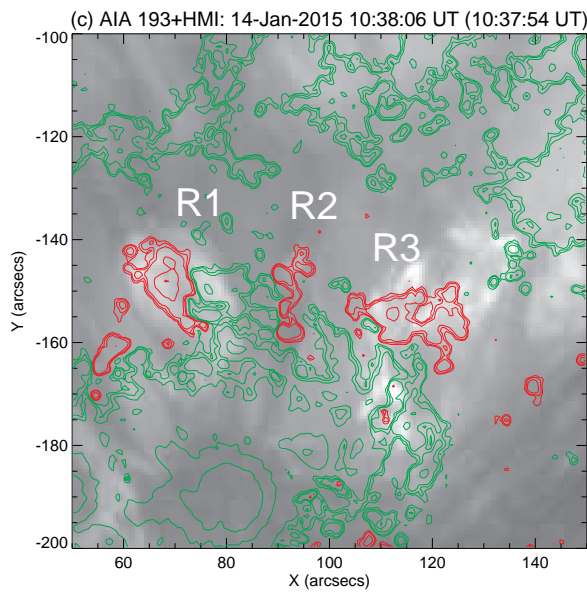
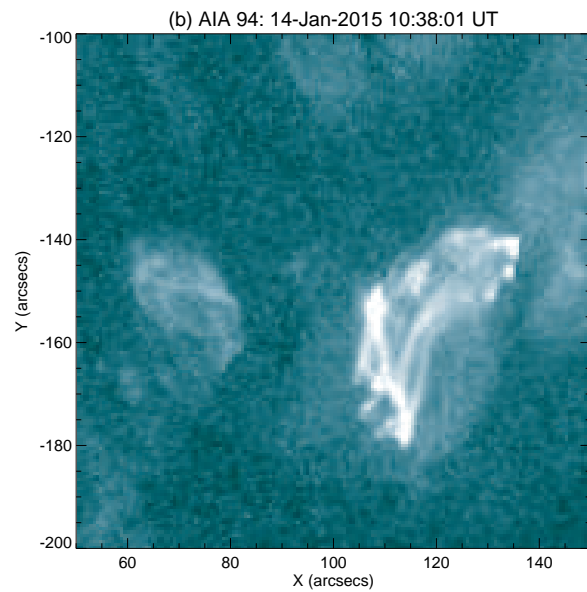
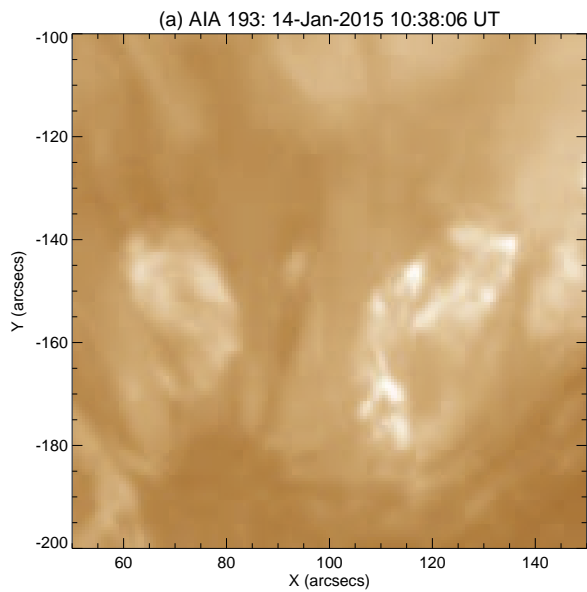


Figure 4

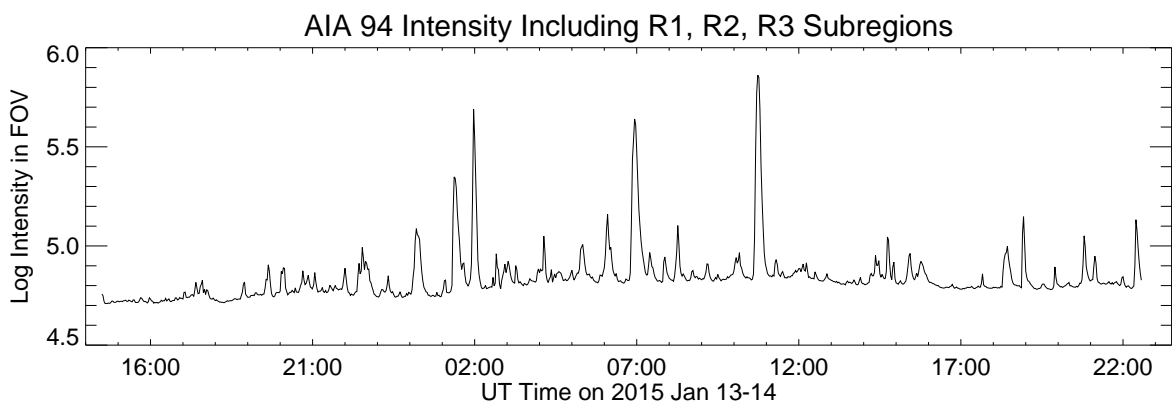


Figure 5

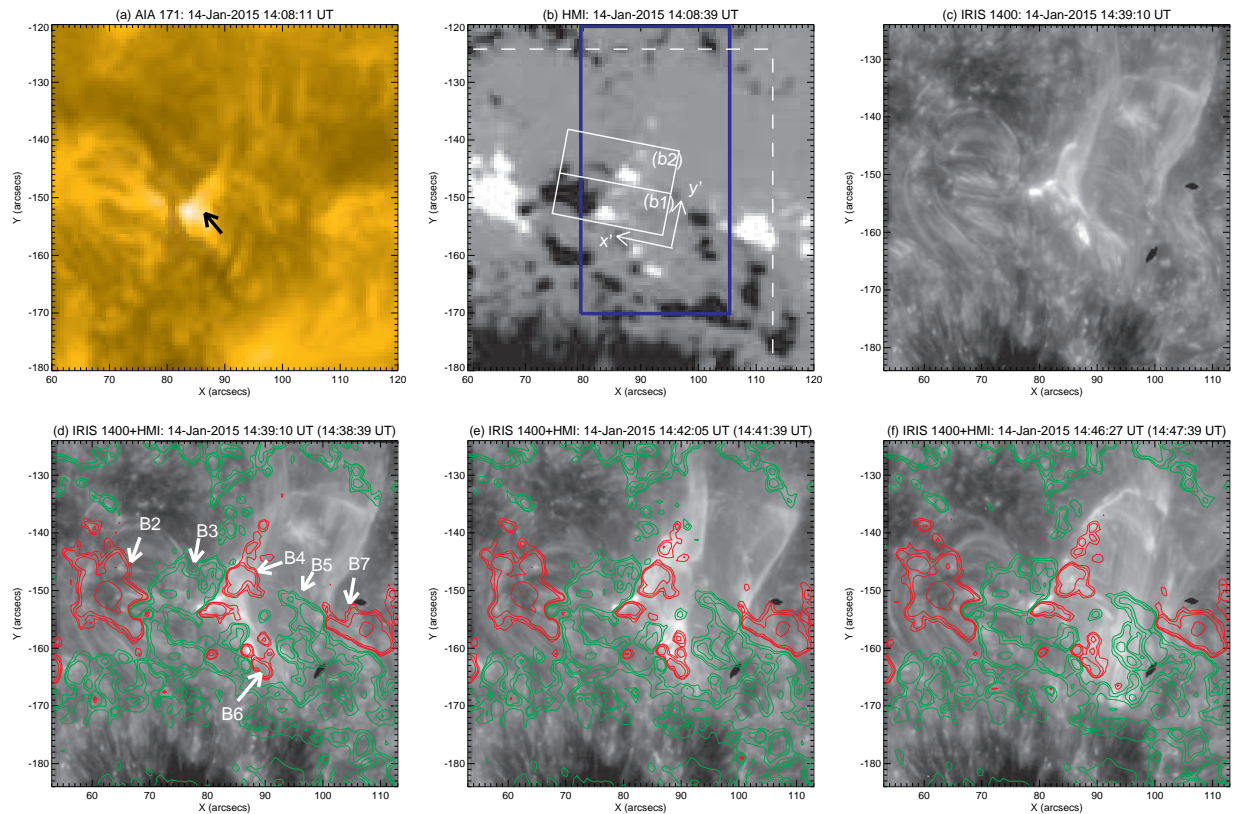


Figure 6

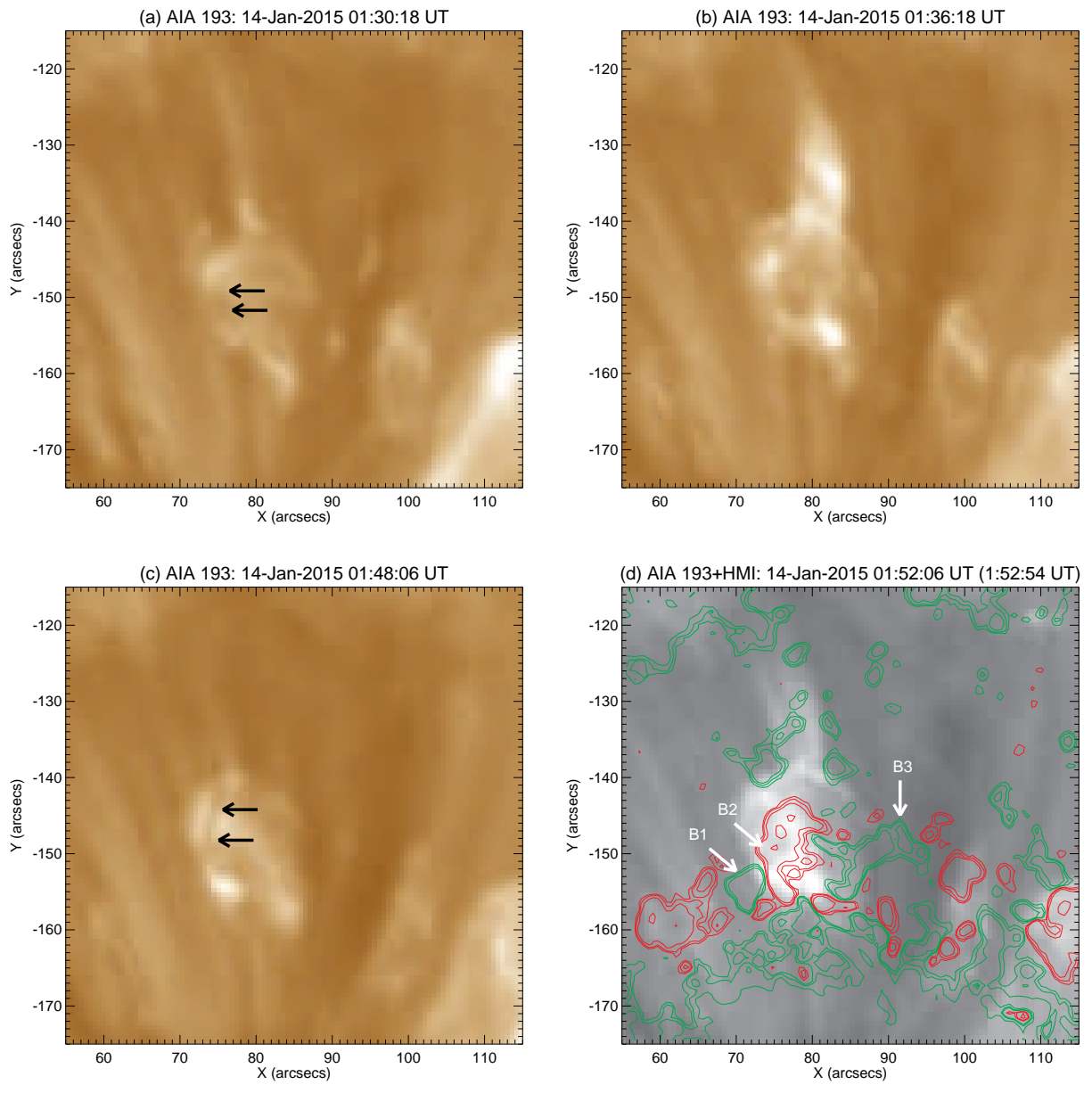


Figure 7

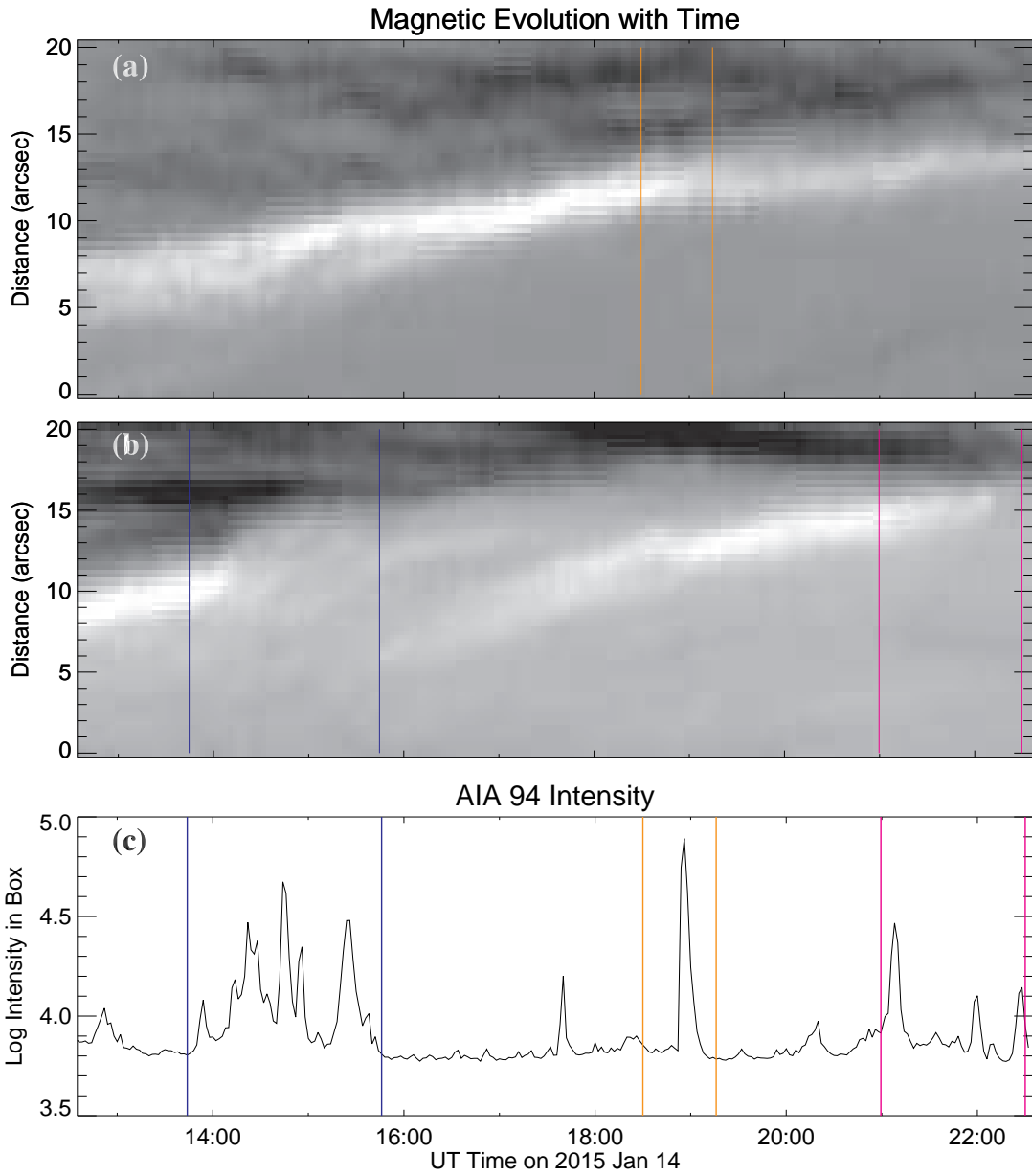


Figure 8

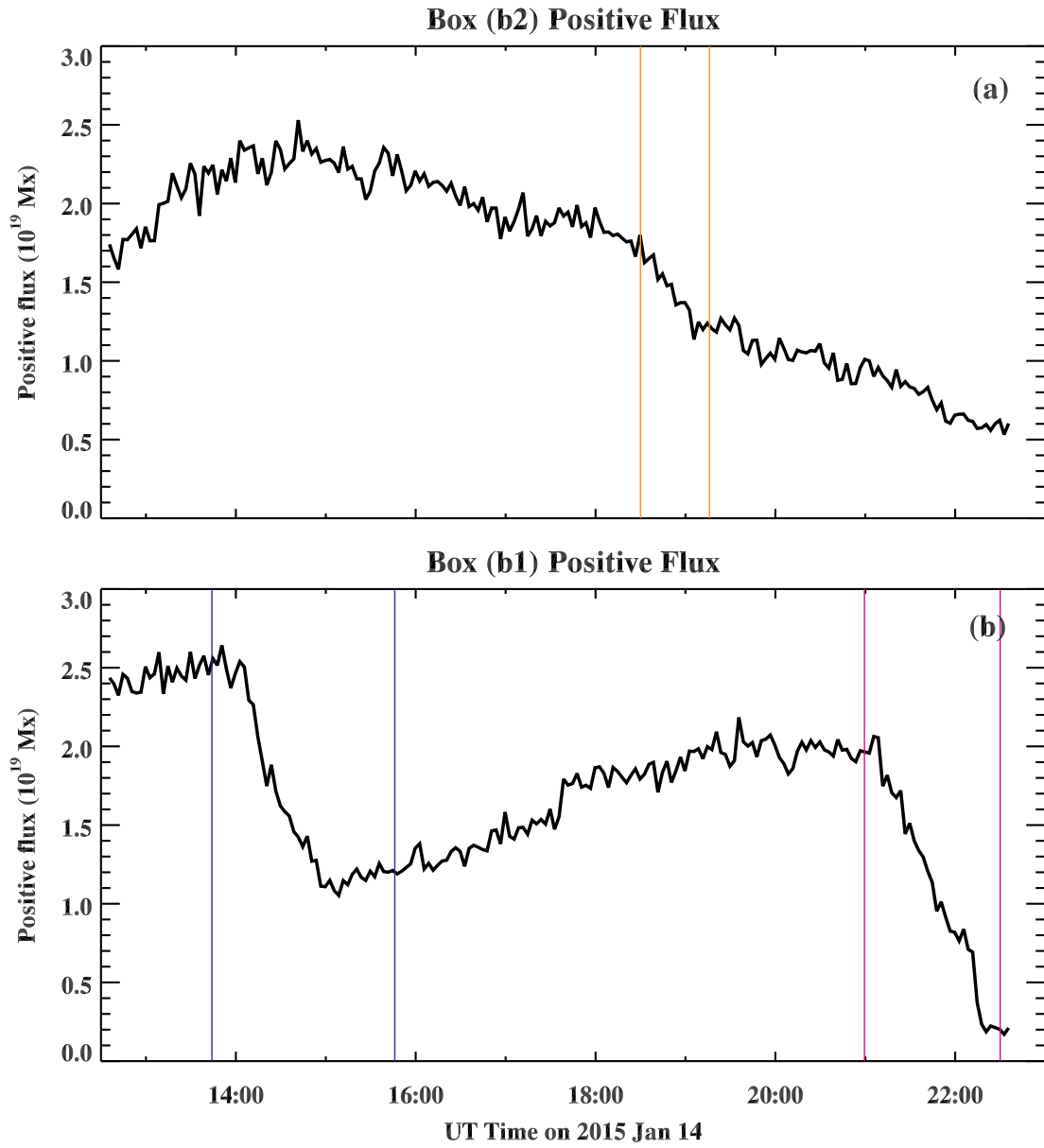


Figure 9